Observation of Rayleigh-Taylor growth to short wavelengths on Nike

C. J. Pawley, S. E. Bodner, J. P. Dahlburg, S. P. Obenschain, A. J. Schmitt, J. D. Sethian, C.A. Sullivan, *Plasma Physics Division, Naval Research Laboratory, Washington, D. C. 20375.*

J. H. Gardner, *Laboratory for Computational Physics and Fluid Dynamics, Naval Research Laboratory, Washington, D. C. 20375*

Y. Aglitskiy, Y. Chan, T. Lehecka, *Science Applications International Corp., McLean, Virginia, 22310*

The uniform and smooth focal profile of the Nike KrF laser [S. Obenschain, *et. al.*, Phys. Plasmas **3**, 1996 (2098)] was used to ablatively accelerate 40 μm thick polystyrene planar targets with pulse shaping to minimize shock heating of the compressed material. The foils had imposed small amplitude sinusoidal wave perturbations of 60, 30, 20, and 12.5 μm wavelength. The shortest wavelength is near the ablative stabilization cutoff for Rayleigh-Taylor growth. Modification of saturated wave structure due to random laser imprint was observed. Excellent agreement was found between the two dimensional simulations and experimental data for most cases where laser imprint was not dominant.
Pacs: 52.35.Py, 52.58.Ns, 52.70.-m

Report Documentation Page

1. REPORT DATE **1999**	2. REPORT TYPE	3. DATES COVERED **00-00-1999 to 00-00-1999**

4. TITLE AND SUBTITLE	5a. CONTRACT NUMBER
Observation of Rayleigh-Taylor growth to short wavelengths on Nike	5b. GRANT NUMBER
	5c. PROGRAM ELEMENT NUMBER
6. AUTHOR(S)	5d. PROJECT NUMBER
	5e. TASK NUMBER
	5f. WORK UNIT NUMBER

7. PERFORMING ORGANIZATION NAME(S) AND ADDRESS(ES) **Naval Research Laboratory,Plasma Physics Division,4555 Overlook Avenue SW,Washington,DC,20375**	8. PERFORMING ORGANIZATION REPORT NUMBER

9. SPONSORING/MONITORING AGENCY NAME(S) AND ADDRESS(ES)	10. SPONSOR/MONITOR'S ACRONYM(S)
	11. SPONSOR/MONITOR'S REPORT NUMBER(S)

12. DISTRIBUTION/AVAILABILITY STATEMENT
Approved for public release; distribution unlimited

13. SUPPLEMENTARY NOTES
This article appeared in Physics of Plasmas and may be found at Phys. Plasmas 6, 565 (1999)

14. ABSTRACT

15. SUBJECT TERMS

16. SECURITY CLASSIFICATION OF:			17. LIMITATION OF ABSTRACT	18. NUMBER OF PAGES	19a. NAME OF RESPONSIBLE PERSON
a. REPORT **unclassified**	b. ABSTRACT **unclassified**	c. THIS PAGE **unclassified**	**Same as Report (SAR)**	**17**	

I. Introduction

The design of direct-drive inertial confinement fusion will require accurate computational modeling of the growth of the ablative Rayleigh-Taylor (R-T) instability[1-6]. There are, however, inevitable approximations and limitations in both the numeric and the physics packages of these simulation codes. The design codes are therefore compared with nearer-term laser-target experiments. For diagnostic access, as well as ease in matching two dimensional (2-D) numerical simulations, experiments frequently use planar targets with imposed one dimensional (1-D) sine wave perturbations[2,7-9]. Recently there have been some doubly-transverse experiments[10] [$\sin(x) \times \sin(y)$], as well as multimode initial perturbations[11]; the linear growth rates for these targets are predicted to be similar to the matching wave number 1-D modes, with differences in the saturation[12,13]. The treatment of random 2-D noise and, in particular, 2-D random laser imprint, is near the limit of experimental [14-17] and numerical[15] capabilities. Accurate modeling of experiments with 2-D (x,y) initial perturbations requires three dimensional (3-D) (x,y,z) radiative hydrodynamic codes with sufficient temporal and spatial resolution that stresses the capabilities of current computers.

We have studied the growth of small amplitude 1-D perturbations[2,14] using the ultra-uniform laser profile of the Nike KrF laser. Despite the improved laser beam uniformity, our experimental images show random 2-D perturbations that arise from both the laser imprint and the target manufacturing flaws. These 2-D imperfections alter the wave structure at saturation.

II Experimental Setup

The experiments described here were performed using nominally 40 μm thick polystyrene [CH] planar targets (density 1 g/cm^3) with planar sinusoidal perturbation wavelengths ranging from 12.5 μm to 60 μm. These wavelengths are believed to cover the interesting range for our experimental conditions, from near the predicted short wavelength cutoff (~7 μm) to longer than the fastest growing modes. The target was positioned with the surface perturbation grooves parallel to the 15° angle between the X-ray diagnostic line of sight and target normal (perturbation wavenumber is perpendicular to the diagnostic plane). This ensured that the diagnostic X-rays did not obliquely intersect the tips of the spike in the highly nonlinear state. The initial perturbation amplitudes were much less than the perturbation wavelength, typically $A_0 = 0.05$ or 0.125 μm. The surface with the perturbations faced the laser drive. The emphasis of our experiment was to study the growth of these waves before saturation effects dominated.

The initial perturbations were too small to be diagnosed with the x-ray system. White light interferometry[18] was therefore used to confirm the initial amplitude of the target surface nonuniformity before each shot.

The laser focus was a 750 μm full-width half-maximum (FWHM) diameter spot with a central 400 μm flat top; the sum of the tilts or lowest-order curvature within the flat top were measured on two beams to be on the order of 5%. The target was driven with 33 of the 56 beams, which reduced the actual tilt and curvature of the total profile on target. The targets were accelerated with 1.6 kJ total, with a nominal peak laser intensity of 7.5×10^{13} W/cm^2.

The laser pulse consisted of a foot pulse followed by a main pulse (see Fig. 1). The amplitude and duration of the foot was designed to significantly reduce the shock heating from the main pulse and allow the target adiabat (pressure divided by Fermi-degenerate pressure) to remain below the value of 3 for the first 3.5 ns of the 4 ns main drive pulse. The foot pulse in this experiment had approximately 4 ns duration, with an amplitude that was 3-5% of the main pulse. At the end of the foot the laser intensity rose to full power in 1 ns. The FWHM of the flat-top main pulse peak power was 4 ns. The time t=0 is defined to be when the main pulse has reached 50% of peak intensity in the rising edge.
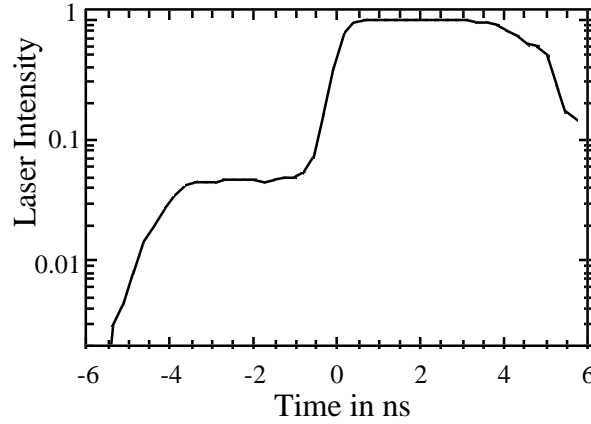

Figure 1. Normalized log plot of the laser intensity at focus versus time for this experiment. Peak intensity is 7.5 x10^{13} W/cm^2. The point where the main drive reaches 50% of peak power in the rising edge is defined as t=0.

One dimensional simulations (FAST1D[19]), using the best estimate of the total laser time history on target (the sum of all 33 beams), is shown in Fig. 2. It can be seen that the shock breakout from the foot pulse occurred 1.5 ns before the main shock. As a result, the back 1/3 of the target decompresses slightly before the main shock recompresses it. This results in a higher isentrope for the rear portion of the target, but leaves the main part of the target at nearly the same isentrope as if the two shocks arrived in unison at the rear of the target. The peak density achieved was only slightly lower than with the ideal timing and so the peak Rayleigh-Taylor growth rate is estimated to be reduced by less than 10%. The initially 40 μm thick targets are still predicted to have compressed to about 10 μm thickness, which is less than the wavelengths of the initial impressed perturbations. The actual laser pulse was used for the simulations, so any small

3

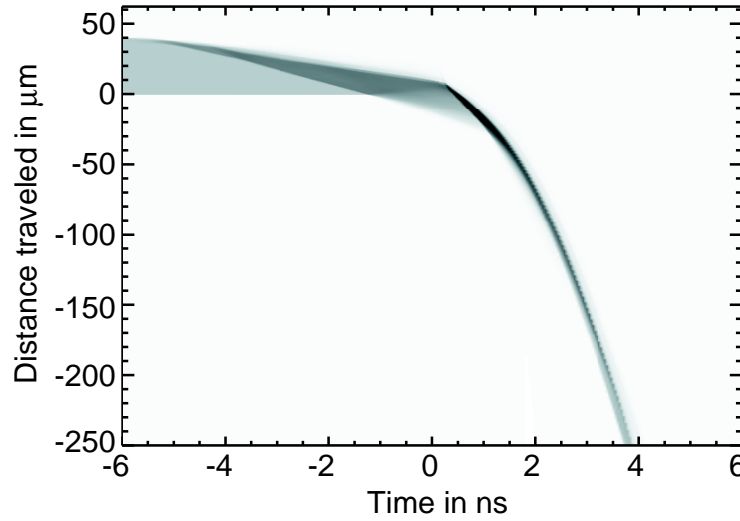changes in the growth rate due to the early foot pulse are accounted for in the simulation results.

Figure 2. One dimensional simulation of the target position as a function of time. Laser drive comes from above. The peak density, achieved at t=0.5 ns, is near 5 g/cm^3.

The target traveled approximately 250 µm by the end of the laser pulse, so there should not be significant target curvature in the central 400 µm of the spot. Side-on imaging was not available for the series of shots reported here, as the twelve laser beams used for x-ray generation were combined to improve the R-T diagnostic. However, this series was virtually identical to previous experiments with side-on steak camera images; those images agreed well with the 1-D simulations.[20]
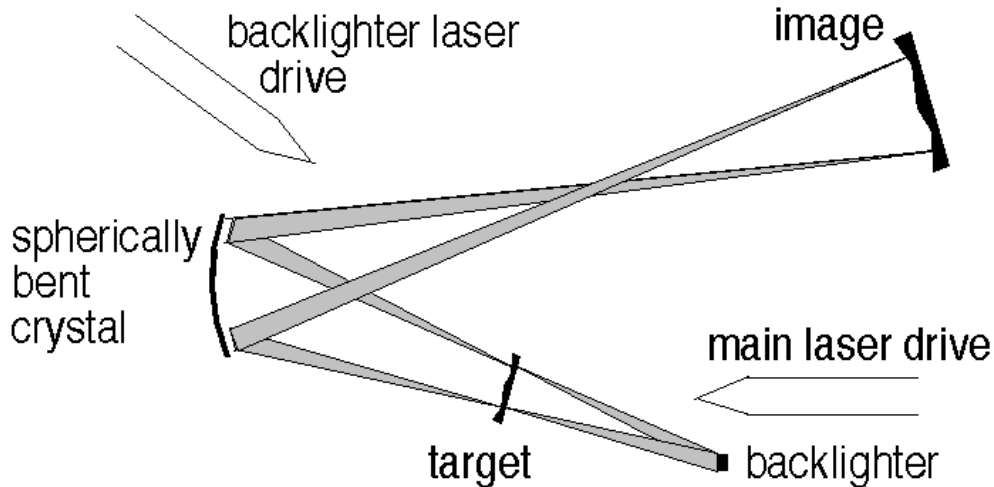

Figure 3. Schematic of experimental layout using the crystal imager. For clarity only one crystal is shown. Spatial scales are distorted as the image is 200 cm away from the crystal, but the crystal is 10 cm from the target.

The primary diagnostic tool for these experiments was an x-ray crystal

imager [21,22] coupled to an x-ray framing camera[23] (see Fig. 3). This diagnostic measured the attenuation of a single spectral line through the target from a backlighter source. The imager was a spherically curved quartz crystal with a curvature radius of 20 cm. The crystal orientation of the quartz reflected the 1.48 keV H-like magnesium lines from the backlighters at a Bragg angle of 6.3 degrees. The reflectivity bandwidth of the crystal is only 0.01-0.02 Å wide; therefore the calculations of the x-ray transmission through the target could assume monochromaticity. We could therefore accurately determine the areal mass redistribution that arises from the Rayleigh-Taylor instability in the cold (< 20 eV), high density portion of the target. Two crystals were used in this experiment to put two 20X magnified images on the framing camera.

The framing camera had four independent gating strips which were driven with 250 ps voltage pulses. The nonlinear dependence of gain on voltage for microchannel plates reduced the effective optical gating time to 200 ps or less. Each image covered two strips, allowing four time frames per shot. As the experiment progressed, crystals were damaged by target debris with some loss of image quality. Crystals were replaced as new ones became available. The resolution and alignment of the system was tracked by a grid shot at the beginning of each day. The total system resolution including the framing camera is shown in Fig. 4.
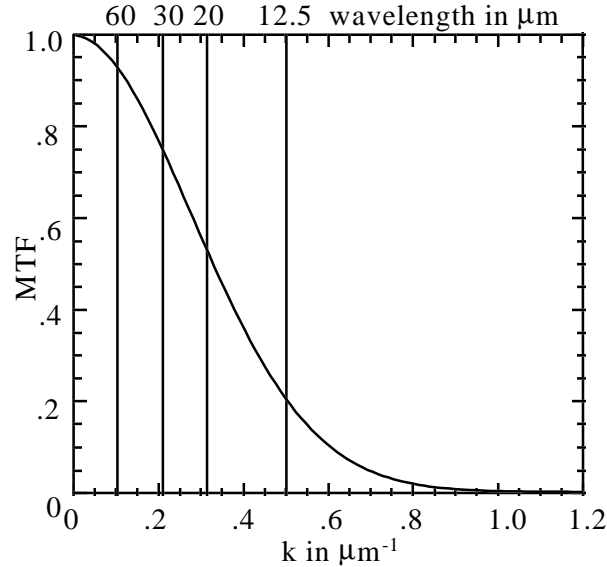

Figure 4. Modulation transfer function derived from a fit to edge resolution data. Lines mark the 4 wavelengths studied in this experiment.
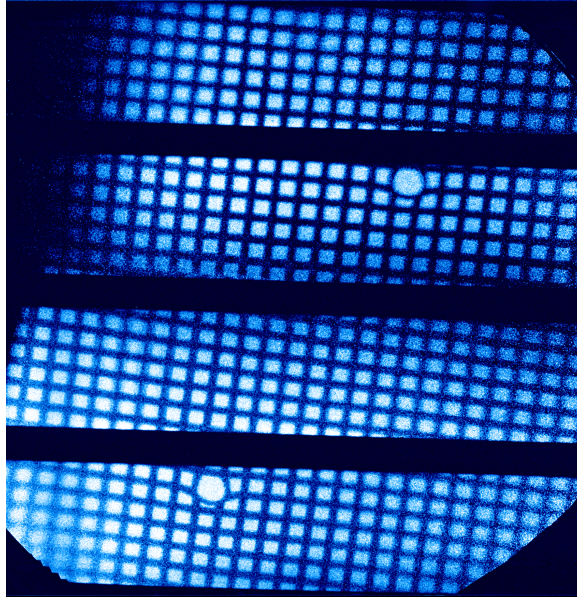
Figure 5. Full image from the X-ray framing camera with the resolution test grid taken each day. There are two images, each spread across two imager strips. The grid wires are thick enough (28 μm) to allow accurate modeling of the point spread function to the edges. The small hole punched in the grid provide a landmark for identifying the center point for laser alignment.

If an image was significantly degraded, those images were dropped from the analysis. A sample framing camera picture using the calibration grid is shown in Fig. 5.

Although the total overlapped Nike laser focal profile is very uniform with short scale length nonuniformities of less than 0.2% rms [24,25] (excluding beam to beam interference at very short scale lengths), there is still some laser imprinting. For our laser drive, and for 40 um thick plastic targets, we have previously shown that the laser imprinting can be numerically modeled as a 100 Å rms random surface perturbation[14]. The modulated targets had machining flaws which were measured by the white light interferometer. We estimate a total noise input (laser imprint plus target flaws) of 150 Å rms, with the largest peak-to-valley modulations reaching 300 to 450 Å. The random structure with spatial frequencies closest to the fastest growing unsaturated R-T modes will appear most clearly in the images. In the experimental images, we observed bubbles 10-20 μm in diameter after 2 ns of the main laser drive. This 2-D structure could interfere with or alter the imposed 1-D perturbations in the nonlinear stage of evolution.

III Simulations

Simulations of the experiments were performed with the Naval Research Laboratory FAST code. Detailed discussion of this code is available in Refs. (26) and (2). The FAST2D code can model the evolution of the ablative and classical Richtmyer-Meshkov[27] [R-M] and Rayleigh-Taylor[5] instabilities, with multi-mode amplitudes that range from the very linear to the strongly nonlinear. The code can treat both initial target mass nonuniformities and laser temporal and spatial nonuniformities as the seeds for the R-M and R-T instabilities. The simulations include spatially nonuniform laser energy deposition, evolution of perturbed shocks and distorted target material interfaces, a multigroup - variable Eddington non-local thermodynamic equilibrium (non-LTE) radiation transport package[28], and tabular real equations of state. FAST is designed to accurately simulate highly nonlinear vortical flows in regions of strong density and pressure gradients needed to model the R-T instability near saturation. Simulation solutions are post-processed to allow direct comparison with data.

IV. Results

Sections of the framing camera digitized film images from which some of the data was obtained are shown in Figs. 6 and 7. Significant 2-D structure is visible in the later time images for all resolved wavelengths, at amplitudes which are larger than the framing camera noise. Figures 8 and 9 shows the experimental data as compared to the simulation results. The data points are obtained by converting the film density to linear light intensity and then taking the logarithm multiplied by the cold opacity for polystyrene. The averaged 1-D Fourier transform of the areal mass density gives the amplitude of the fundamental and harmonics. The simulation calculates a 2-D mass distribution which is post processed by calculating the x-ray line of sight absorption, then taking the Fourier transform of the transmitted x-ray intensity. The framing camera modulation transfer function (MTF) is multiplied to the transform and the inverse transform returns the simulated light intensity distribution at the camera. As with the experimental data, the mass density structure is recreated and the Fourier components are found. Each plot shows both the averaged fundamental and second harmonic Fourier amplitudes of the sine wave perturbations for each time resolved image as well as the 2-D simulation prediction with and without MTF correction. The solid points on the plots are the data obtained for the specific experimental measured time history used in the simulation. All other points are from shots which were very similar. Error bars of $\pm\,25\,\%$ have been assigned to the data points due to the significant averaging over the vertical direction required to reduce camera noise. This also averages the effect of laser imprint which will increase scatter in the data.

Figure 8 shows the results for 60 and 30 μm wavelength cases. The growth rates predicted by the code agree with the data for the 60 and 30 μm wavelength perturbations. Some of the discrepancy between the data and simulation is the
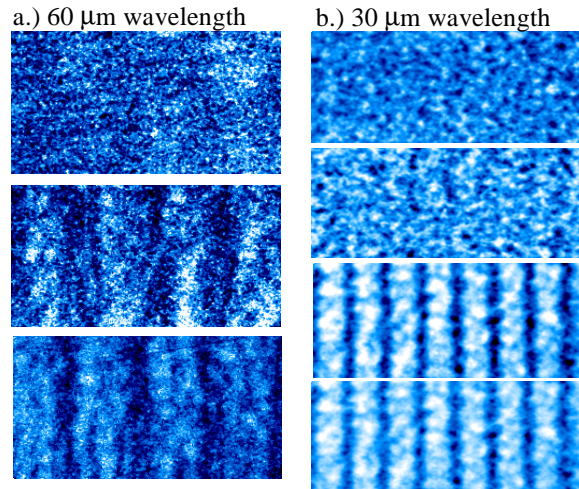
7

a.) 60 µm wavelength   b.) 30 µm wavelength

Figure 6. Image sections used for analysis of a) 60 µm wavelength sine wave, and b) 30 µm wavelength sine wave. In a) the times are (from top to bottom): 2.07 ns, 2.57 ns, and 3.17 ns. In b) the times are: 0.87ns, 1.52 ns, 1.72 ns, and 2.37 ns.
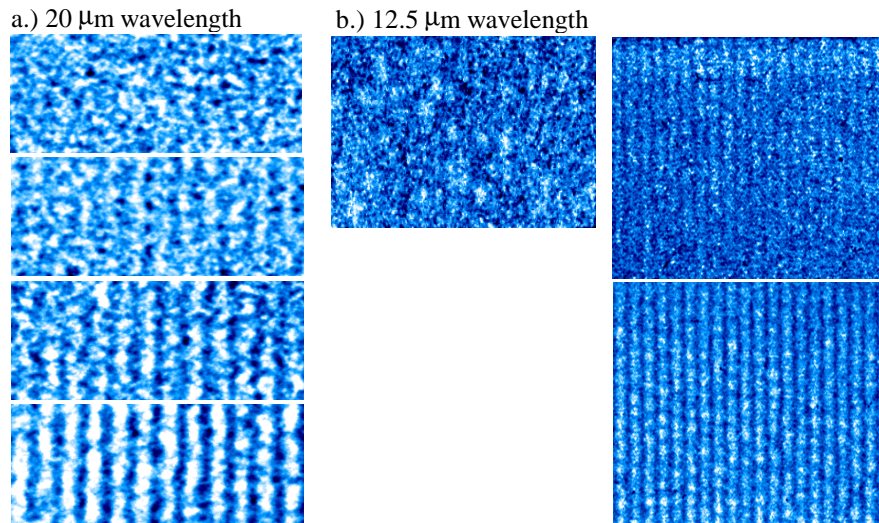
a.) 20 µm wavelength   b.) 12.5 µm wavelength

Figure 7. Image sections used for analysis of a) 20 µm wavelength sine wave, and b) 12.5 µm wavelength sine wave. In a) the time are (from top to bottom): 0.87 ns, 1.52 ns, 1.92 ns, and 2.57 ns. In b) the times are 1.52 ns and 2.17 ns.

Please note the new images added alongside the original images used in the paper. These are from a much later run (Feb. of 1999) with twice the spatial resolution and lower noise. The 12.5 um wavelength is growing at the predicted rate and saturates at the amplitude predicted. The earlier data was not absolutely conclusive on this issue.
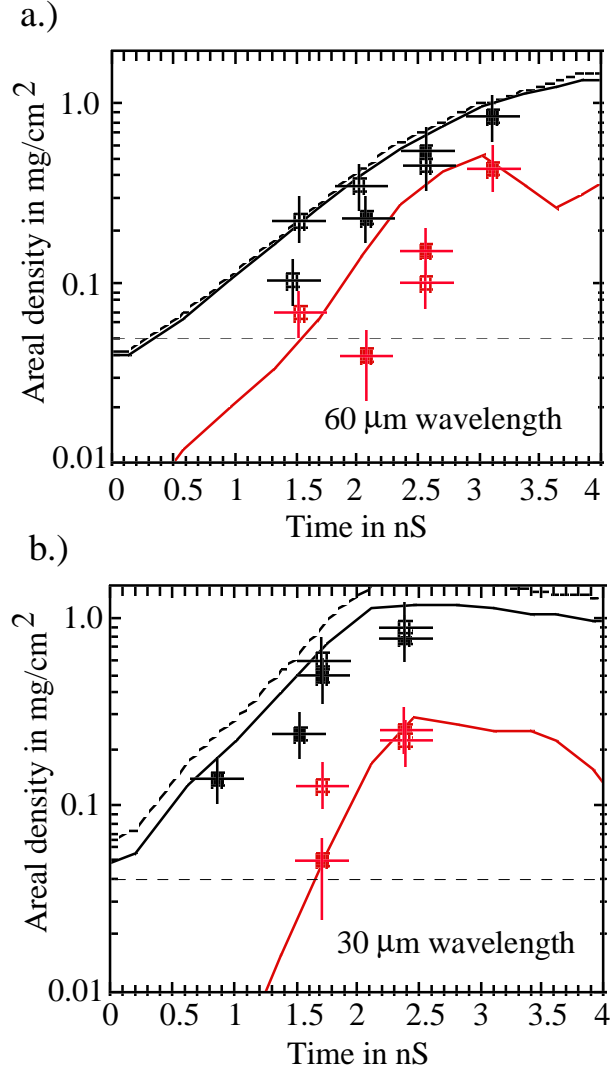
Figure 8. The Fourier amplitude for the first and second harmonics (black and red, respectively) of the areal mass density from the simulation, multiplied by the MTF. The dashed black line is the Fourier amplitude of the fundamental without the MTF correction, showing the size of the reduction. The closed boxes are experimental data from the specific laser shot simulated, open symbols are from similar shots. The 60 μm wavelength results are in a); the 30 μm wavelength results are in b). The initial amplitude in both cases is 0.125 μm.
Error bars are ± 200 ps in the horizontal and ± 25% in the vertical. The noise floor for the fundamental wavelength is shown as a dashed line.
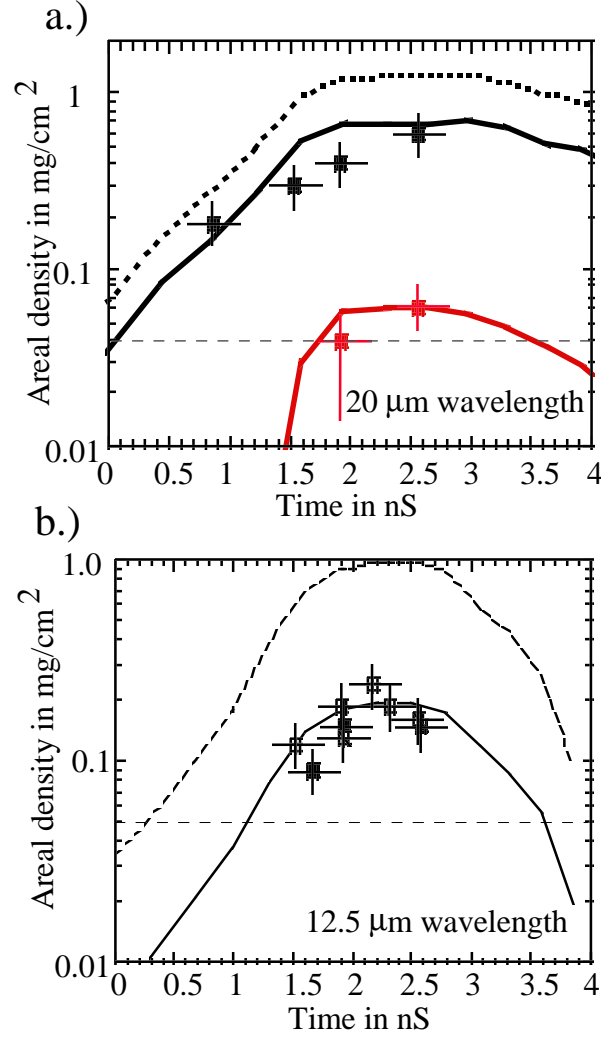
Figure 9. The Fourier amplitude for the first and second harmonics (black and red, respectively) of the areal mass density from the simulation, multiplied by the MTF. The dashed black line is the Fourier amplitude of the fundamental without the MTF correction, showing the size of the reduction. The closed boxes are experimental data from the specific laser shot simulated, open symbols are from similar shots. The 20 μm wavelength results are in a); the 12.5 μm wavelength results are in b). The initial amplitude in both cases is 0.125 μm. Error bars are ± 200 ps in the horizontal and ± 25% in the vertical. The noise floor for the fundamental wavelength is shown as a dashed line.

uncertainty in determining the frame times of the camera; timing checks performed on the camera are within the ±200 ps error of the digitizing oscilloscopes used to obtain the timing, X-ray, and optical signals. Larger scatter in the data is noticeable for the 60 μm data due it's slower growth rate making initial conditions more important and increased competition from laser imprint.

Figure 9 shows the results for the 20 and 12.5 μm wavelength cases. The MTF correction is larger for these shorter wavelengths and thus errors in determining the MTF are important. For our best estimate of the MTF, using a gaussian fit to model grid wire resolution for two sizes of wire, the data continues to agree with the simulation.
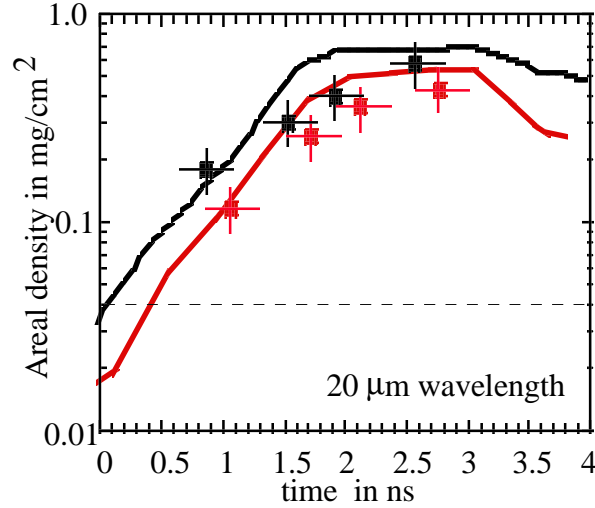

Figure 10. Comparison of the simulation results and the experimental data of the Fourier amplitude of the 20 μm wavelength for the initial amplitude of 0.125 μm (black curve and boxes) and 0.05 μm (red curve and boxes). Error bars are ± 200 ps in the horizontal and ± 25% in the vertical. The noise floor for the fundamental wavelength is shown as a dashed line.

Figure 10 shows the effect of reducing the initial amplitude of the 20 μm perturbation from 0.125 μm to 0.05 μm. A reduced initial perturbation amplitude should introduce a time delay to when the perturbations reach an experimentally observable amplitude. The first three data points, when fitted to a straight line, give a 400 ps delay. The 2-D simulation predict a 350 ps delay, in reasonable agreement with the code.

Between 0 and +2 ns the RT growth rate for each wavelength predicted by the FAST2D code can be closely approximated by using the FAST1D code to find the acceleration g and ablation velocity $V_{ab} = \dot{m} / \rho_{peak}$ with the ablative and profile stabilization model[29,30,5] $\gamma = \sqrt{\dfrac{\kappa\gamma}{1+\alpha\kappa\Lambda}} - \beta\,\kappa\varsigma_{ab}$, ωιτη α=0.2, and β=3. The agreement with a simple analytical model indicates that, in the simulation, saturation effects do not alter the perturbation growth rate early in the pulse and

that the target adiabat is not changing rapidly in this time window. The above formula predicts that the 60 μm wavelength growth rate is 80% of $\sqrt{kg}$, while the 12.5 μm growth rate is reduced to 50% of $\sqrt{kg}$, mostly due to the ablative stabilization term. For wavelengths shorter than 12.5 μm, the ablative stabilization term will increase faster than the classical growth rate, resulting in a lower total growth rate. Therefore, the experimental results covers all of the fastest growing modes.

The random 2-D (x,y) perturbations caused by laser imprint and target nonuniformities will grow along with the impressed 1-D (x) modes. The model for the laser imprint used in the 2-D (x,z) code is based on the theoretical and measured laser focal profile created by induced spatial incoherence (ISI) optical smoothing on Nike.[24,25] Using this ISI model, the 2-D (x,z) simulations predict that the laser imprint on a perfectly flat target, amplified by the R-T instability, will be dominated by 20-30 μm modes. It can be expected that the actual 3-D (x,y,z) modes would predominantly produce round bubbles in the targets with similar wave number spectra. The largest growth rate of an imprint bubble can be estimated by modeling it as a Bessel function $J_0(kr)$ with $k=2\pi/20$ μm^{-1} . Three dimensional simulations show the growth rate for this Bessel bubble to be at least as large as for a 20 μm 1-D sine wave[13], and the bubble will saturate at a far larger amplitude than the sine wave.

The late time images in Fig. 6a for the 60 μm case show that the trough of the imposed perturbation has been divided into 20 μm troughs. This is not a normal saturation mode for an R-T amplified sine wave. The division can be explained by the merging of the faster growing 20 μm ISI bubbles with the 60 μm sinusoid, resulting in the bubbles being tiled into a regular perturbation which develops into the observed trough cutting mode. The linear growth rate of the bubbles is approximately 1.4 times larger than the 60 μm 1-D mode, so the 2-D bubbles will reach comparable amplitudes by 2 ns into the main drive, and begin to nonlinearly interact with the impressed mode. The tiling effect is a nonlinear interaction between the two modes.

Figure 11 shows a simulation image of the spatial density distribution of the 60 μm wavelength mode (including ISI fluctuations) at 3 ns, with the corresponding simulation of the X-ray diagnostic lineout path and the camera MTF. At the bottom is a selected lineout from the experimental image at 3.17 ns converted to the mass perturbation and set to have the same average density as the simulation. Our ability to match an experimental lineout to the simulation shows that the code is reasonably modeling the tiled 20 μm bubbles coupling into the 60 μm wave.
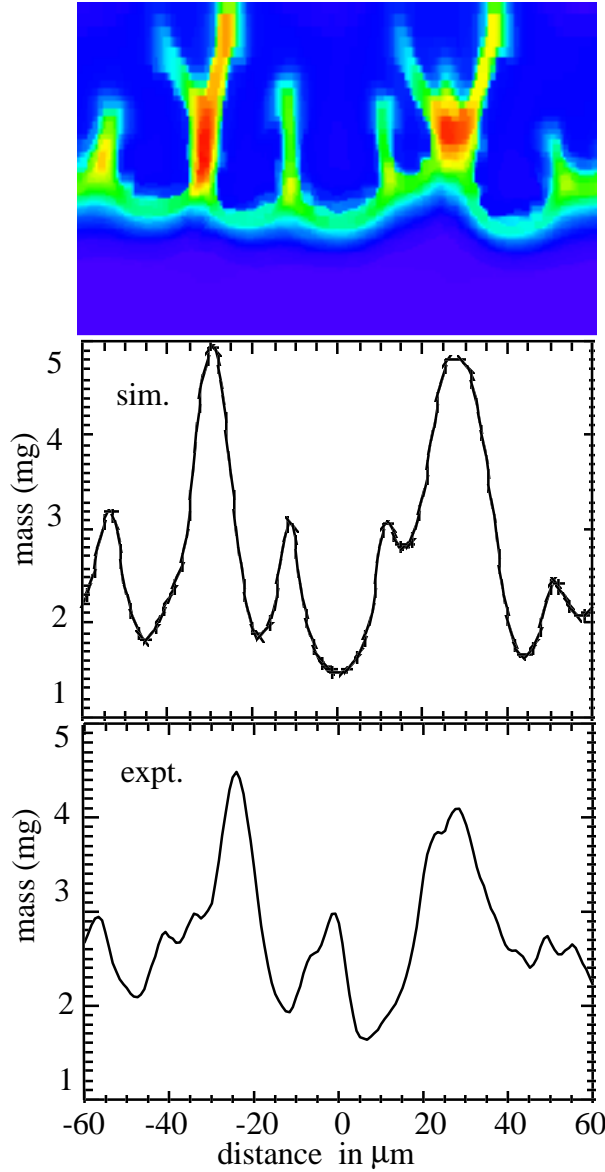
Figure 11 a) The density distribution in the target at 3.0 ns from the simulation of the 60 μm wavelength case. b) The simulated framing camera lineout of this simulation accounting for the integration along the X-ray path and the camera MTF. c) A selected subsection lineout from the image in Fig. 6a which resembles the simulation result.

The experimental images also show that the 2-D laser imprinting has coupled into the impressed shorter wavelength 1-D modes. The 30 μm wavelength images in Fig. 6b show that the laser imprint is well matched to the sine wave and again the bubbles tile into the trough late in time. The 20 μm wavelength images in Fig. 7a show that laser imprint is beginning to distort the straight walls of the sine wave perturbation, causing the walls to bend and break up. The saturated behavior of 1-D and 2-D modes is different. As the 1-D (x) sine wave

13

mode saturates into broad flat troughs with thin walls between, the bubble will continue to grow at the fast linear rate, allowing the initially smaller perturbation (400 Å) to catch up to and exceed the amplitude of the 1-D mode. Such bubbles will curve and tip the walls of the 1-D perturbation. This will be important to the shortest wavelength 1-D modes since these walls can be very thin as the wave reaches saturation; simulations of the 12.5 μm sine wave show the walls being only 3-4 μm thick in saturation. The larger scatter in the 12.5 μm data amplitude in Fig. 9b is mostly due to the interference of the random laser imprint. Also, in Fig. 10, the larger disagreement for the .05 μm initial amplitude case versus the .125 μm initial amplitude case is at least partially due to competition with laser imprint, since the laser imprint in the later time images was clearly visible.

V. Summary

The simulation results are in good agreement with the experiments for all the perturbation wavelengths. The mass imprinting from the random ISI laser perturbations produces visible effects in all cases. These effects are adequately handled by the 1-D imprint model in simulations when the bubbles tile into the wavelength troughs, as evidenced by the agreement with the data. Departure from the predicted amplitudes will occur if 2-D mode structure reaches saturation amplitudes where the 2-D structures will dominate. Interaction between the 1-D and 2-D modes is experimentally observed both in the case where the 2-D mode growth is faster than the impressed mode (60 μm sine wave) and where the growth rates should be comparable (20 μm sine wave). The nonlinear interaction of the 1-D and 2-D alters the saturated behavior of both modes.

VI. Acknowledgment

References

1. S. E. Bodner, D. G. Colombant, J. H. Gardner, R. H. Lehmberg, S. P. Obenschain, L. Phillips, A. J. Schmitt, J. D. Sethian, R. L. McCrory, W. Seka, C. P. Verdon, J. P. Knauer, B. B. Afeyan, H. T. Powell, *Phys. Plasmas*, **5**,1901 (1998).

2. J. H. Gardner, A. J. Schmitt, J. P. Dahlburg, C. J. Pawley, S. E. Bodner, S. P. Obenschain, V. Serlin, Y. Aglitskiy, *Phys. Plasmas*, **5**, 1935 (1998).

3. R. L. McCrory, and C. P. Verdon, "Computer Modeling and Simulation in Inertial Confinement Fusion," International School of Plasma Physics Piero Caldirola: Inertial Confinement Fusion (1988), edited by A. Caruso and E. Sindoni (Editrice Compositori, Bologna, Italy, 1988), pp. 83-124.

4. J. Lindl, *Phys.Plasmas*, **2**, 3933 (1995).

5. J. H. Gardner, S. E. Bodner, J. P. Dahlburg, *Phys. Fluids B*, **3**, 1070 (1991).

6. J. Nuckolls, L. Wood, A. Thiessen, and G. Zimmerman, *Nature*, **239**, 139 (1972); D.H.Sharp, *Physica* **12D**, 3 (1984).

7. B. A. Remington, S. V. Weber, S.W. Haan, J.D. Kilkenny, S. G. Glendinning, R. J. Wallace, W. H. Goldstein, B. G. Wilson, J. K. Nash, *Phys. Fluids B*, **5**, 2589 (1993).

8. S. G. Glendinning, S. N. Dixit, B. A. Hammel, D. H. Kalantar, M. H. Key, J. D. Kilkenny, J. P. Knauer, P. M. Pennington, B. A. Reminton, R. J. Wallace, S. V. Weber, *Phys. Rev. Lett.*, **78**, 3318 (1997).

9. H. Azechi, M. Nakai, K. Shigemori, N. Miyanaga, H. Shiraga, H. Nishimura, M. Honda, R. Ishizaki, J. G. Wouchuk, H. Takabe, K. Nishihara, K, Mima, A. Nishiguchi, T. Endo, *Phys.Plasmas*, **4**, 4079 (1997).

10. M. M. Marinak, B. A. Remington, S. V. Weber, R. E. Tipton, S. W. Haan, K. S. Budil, O. L. Landen, J. D. Kilkenny, R. Wallace, *Phys. Rev. Lett.*, **75**, 3677 (1995).

11. M. M. Marinak, S. G. Glendinning, R. J. Wallace, B. A. Remington, K. S. Budil, S. W. Haan, R. E. Tipton, J. D. Kilkenny, *Phys. Rev. Lett.*, **80**, 4426 (1998).

12. J. P. Dahlburg, J. H. Gardner, *Physical Rev. A*, **41**, 5695, (1990).

13. J. P. Dahlburg, J. H. Gardner, G. D. Doolen, S. W. Haan, *Phys. Fluids B*, **5**, 571 (1993); J. P. Dahlburg, D. E. Fyfe, J. H. Gardner, S. W. Haan, S. E. Bodner, G. D.

Doolen, *Phys.Plasmas*, **2**, 2453 (1995).

14. C. J. Pawley, K. Gerber, R. H. Lehmberg, E. A. McLean, A. N. Mostovych, S. P. Obenschain, J. D. Sethian, V. Serlin, J. A. Stamper, C. A. Sullivan, S. E. Bodner, D. Colombant, J. P. Dahlburg, A. J. Schmitt, J. H. Gardner, C. Brown, J. F. Seely, T. Lehecka, Y. Aglitskiy, A. V. Deniz, Y. Chan, N. Metzler, and M. Klapisch, *Phys.Plasmas*, **4**, 1969 (1997).

15. R. J. Taylor, J. P. Dahlburg, A. Iwase, J. H. Gardner, D. E. Fyfe, O. Willi, *Phys. Rev. Lett.*, **76**, 1643 (1996).

16. S. G. Glendinning, S. N. Dixit, B. A. Hammel, D. H. Kalantar, M. H. Key, J. D. Kilkenny, J. P. Knauer, P. M. Pennington, B. A. Remington, J. Rothenberg, R. J. Wallace, S. V. Weber, *Phys. Rev. Lett.*, **80**, 1904 (1998).

17. D. H. Kalantar, M. H. Key, L. B. DaSilva, S. G. Glendenning, J. P. Knauer, B. A. Remington, F. Weber, and S. V. Weber, *Phys. Rev. Lett.*, **76**, 3574 (1996).

18. Details available from Phase Shift Technology, Inc., 1430 East Fort Lowell, Tuscon, Arizona 85719

19. J.H. Gardner and S.E. Bodner, Phys. of Fluids **29**, 2672 (1986).

20. V. Serlin, S. P. Obenschain, J. D. Sethian, E. A. McLean, J. P. Dahlburg, A. J. Schmitt, J. H. Gardner, T. Lehecka, A. V. Deniz, *Bull.Am.Phys.Soc.*, **42**, 1892 (1997).

21. Y.Aglitskiy, T. Lehecka, A. Deniz, J. Hardgrove, J. Seely, C. Brown, U. Feldman, C. Pawley, K. Gerber, S. Bodner, S. Obenschain, R. Lehmberg, E. McLean, M. Pronko, J. Sethian, J. Stamper, A. Schmitt, C. Sullivan, G. Holland, and M. Laming, *Rev.Sci.Instrum.*, **68**, 806 (1997).

22. Y.Aglitskiy, T. Lehecka, S. Obenschain, S. Bodner, C. Pawley, K. Gerber, J. Sethian, C. Brown, J. Seely, U. Feldman, G. Holland *Applied Optics*, **37**, 5253 (1998).

23. O.L. Landon, P.M. Bell, J.J. Satariano, J.A. Oertel, D.K. Bradley, *Ultrahigh and High-Speed Photography, Videography, and Photonics '93*, SPIE Proc. No. 2002 (SPIE, Bellingham, WA 1995) p.1; K.S. Budil, T.S. Perry, P.M. Bell J.D. Hares P.L. Miller, T.A. Peyser, R. Wallace, H. Louis, D.E. Smith, *Rev. of Sci. Instrum*. **67**, 485 (1996).

24. S. P. Obenschain, S. E. Bodner, D. Colombant, K. Gerber, R. H. Lehmberg, E. A. McLean, A. N. Mostovych, M. S. Pronko, C. J. Pawley, A. J. Schmitt, J. D. Sethian, V. Serlin, J. A. Stamper, and C. A. Sullivan, J. P. Dahlburg, J. Gardner, Y. Chan, A.V. Deniz, J. Hardgrove, T. Lehecka, and M. Klapish, *Phys. Plasmas,* **3**, 2098 (1996).

25. A.V. Deniz, T. Lehecka, R. H. Lehmberg, S. P. Obenschain *Optics Comm.*, **147**, 402 (1998).

26. M. H. Emery, J. P. Boris, and J. H. Gardner, *Appl. Phys. Lett.*, **41**, 808 (1982).

27. R. D. Richtmyer, *Comm. Pure Appl. Math.*, **13**, 297 (1960); E. E. Meshkov, *Fluid Dyn.*, **4**(5), 101 (1969).

28. J. P. Dahlburg, M. Klapisch, J. H. Gardner, A. J. Schmitt, and A. Bar-Shalom, *J. Quant.Spectros. Radiat. Transfer*, **54**, 113 (1995).

29. S. E. Bodner, *Phys.Rev.Lett.*, **33**, 761 (1974); H. Takabe, K. Mima, L. Montierth, and R. L. Morse, *Phys. Fluids*, **28**, 3676 (1985).

30. M. Tabak, D. H. Munro, J. D. Lindl, *Phys. Fluids B*, **2**, 1007 (1990).